Multiple variants of the fungal effector AVR-Pik bind the HMA domain of the rice protein OsHIPP19, providing a foundation to engineer plant defense

Josephine H.R. Maidment[1] [iD], Marina Franceschetti[1] [iD], Abbas Maqbool[1] [iD], Hiromasa Saitoh[2] [iD],
Chatchawan Jantasuriyarat[1,3,4] [iD], Sophien Kamoun[5] [iD], Ryohei Terauchi[6,7] [iD], and Mark J. Banfield[1,*] [iD]

From the [1]Department of Biological Chemistry, John Innes Centre, Norwich Research Park, Norwich, UK; [2]Department of Molecular Microbiology, Faculty of Life Sciences, Tokyo University of Agriculture, Tokyo, Japan; [3]Department of Genetics, Faculty of Science, [4]Center for Advanced Studies in Tropical Natural Resources, National Research University-Kasetsart University (CASTNAR, NRU-KU), Kasetsart University, Bangkok, Thailand; [5]The Sainsbury Laboratory, University of East Anglia, Norwich Research Park, Norwich, UK; [6]Division of Genomics and Breeding, Iwate Biotechnology Research Centre, Iwate, Japan; [7]Laboratory of Crop Evolution, Graduate School of Agriculture, Kyoto University, Kyoto, Japan

Edited by Joseph Jez

Microbial plant pathogens secrete effector proteins, which manipulate the host to promote infection. Effectors can be recognized by plant intracellular nucleotide-binding leucine-rich repeat (NLR) receptors, initiating an immune response. The AVR-Pik effector from the rice blast fungus *Magnaporthe oryzae* is recognized by a pair of rice NLR receptors, Pik-1 and Pik-2. Pik-1 contains a noncanonical integrated heavy-metal-associated (HMA) domain, which directly binds AVR-Pik to activate plant defenses. The host targets of AVR-Pik are also HMA-domain-containing proteins, namely heavy-metal-associated isoprenylated plant proteins (HIPPs) and heavy-metal-associated plant proteins (HPPs). Here, we demonstrate that one of these targets interacts with a wider set of AVR-Pik variants compared with the Pik-1 HMA domains. We define the biochemical and structural basis of the interaction between AVR-Pik and OsHIPP19 and compare the interaction to that formed with the HMA domain of Pik-1. Using analytical gel filtration and surface plasmon resonance, we show that multiple AVR-Pik variants, including the stealthy variants AVR-PikC and AVR-PikF, which do not interact with any characterized Pik-1 alleles, bind to OsHIPP19 with nanomolar affinity. The crystal structure of OsHIPP19 in complex with AVR-PikF reveals differences at the interface that underpin high-affinity binding of OsHIPP19-HMA to a wider set of AVR-Pik variants than achieved by the integrated HMA domain of Pik-1. Our results provide a foundation for engineering the HMA domain of Pik-1 to extend binding to currently unrecognized AVR-Pik variants and expand disease resistance in rice to divergent pathogen strains.

* For correspondence: Mark J. Banfield, mark.banfield@jic.ac.uk.
Present address for Josephine H.R. Maidment: The Sainsbury Laboratory, University of East Anglia, Norwich Research Park, Norwich NR4 7UH, UK.
Present address for Abbas Maqbool: The Sainsbury Laboratory, University of East Anglia, Norwich Research Park, Norwich NR4 7UH, UK.

Phytopathogens constrain crop production and threaten global food security. The filamentous ascomycete fungus *Magnaporthe oryzae* is the causative agent of rice blast disease, which annually destroys enough rice to feed upward of 200 million people for a year (1, 2). *M. oryzae* is found in all major rice-growing regions around the world (3), and severe epidemics can cause total crop loss (2, 4). In addition to rice, strains of *M. oryzae* can infect and cause blast disease on other staple food crops such as wheat, barley and millet, and various wild grass species (5, 6).

During infection, phytopathogens deliver effector proteins to the plant apoplast and to the inside of host cells. These effectors function in diverse ways to suppress immunity and manipulate endogenous processes to create favorable conditions for colonization. While many *M. oryzae* effector candidates have been identified and cloned (7), only a few have been functionally characterized (8–13). For most *M. oryzae* effectors described to date, the mechanism by which they promote fungal virulence remains unknown.

The presence of some effectors inside host cells can be detected by specific nucleotide-binding, leucine-rich repeat domain containing proteins (NLRs) (14). NLRs are intracellular immune receptors, which instigate defensive signaling pathways following perception of a specific effector protein, either through direct interaction with the effector or through monitoring the state of an intermediate protein (15–17). The canonical NLR structure comprises a C-terminal leucine-rich repeat domain, a central nucleotide-binding NB-ARC domain, and an N-terminal coiled-coil (CC or CC_R (18)) or Toll/interleukin-1 receptor (TIR) domain (19–21). Recent studies have identified noncanonical domains in multiple NLR proteins from different plant species (22–24). These integrated domains (IDs) are thought to have their evolutionary origins in the host targets of the effector (25, 26). By acting as an effector substrate or interactor, they enable the NLR to detect the presence of the effector and trigger host immunity.

Interaction between AVR-Pik effectors and OsHIPP19

The paired rice CC-NLRs Pik-1 and Pik-2 are genetically linked and cooperate to trigger immunity in response to the *M. oryzae* effector AVR-Pik (27–29). Pik-1 contains an integrated heavy-metal-associated (HMA) domain between the canonical CC and NB-ARC domains (29). Previous work demonstrated that detection of AVR-Pik is through direct binding of the effector to the integrated HMA domain of Pik-1 (29). Five Pik-1 alleles have been identified and cloned (27, 30–32), with most polymorphisms located in and around the integrated HMA domain. The integrated HMA domain of Pik-1 is thought to resemble the host target of AVR-Pik. While it has been speculated that AVR-Pik may target rice proteins containing an HMA domain (33), until recently (34) these targets have remained undefined.

Six AVR-Pik variants (A–F) have been identified to date, differing in just five amino acid positions (28, 35–37). Each of these polymorphic amino acids is located at the interface with Pik-1-HMA (29), indicating that they are adaptive. While *M. oryzae* strains carrying AVR-PikD trigger immune responses in rice lines containing Pikp, Pikm, Pikh, or Pik*, strains carrying either AVR-PikE or AVR-PikA only elicit a response in rice lines with Pikm or Pikh (28, 29, 36, 38). No known naturally occurring Pik alleles respond to the stealthy effectors AVR-PikC and AVR-PikF.

In an independent study (34), rice proteins targeted by the AVR-PikD effector were identified by a yeast two-hybrid screen. Four small heavy-metal-associated domain-containing (sHMA) proteins were identified as interactors of AVR-PikD. OsHIPP19 (LOC_Os04g39350) and OsHIPP20 (LOC_Os04g39010) are members of the heavy-metal-associated isoprenylated plant protein (HIPP) family (39, 40), while OsHPP03 (LOC_Os02g37290) and OsHPP04 (LOC_Os02g37300) belong to the heavy-metal-associated plant protein (HPP) family. All four proteins contain an N-terminal HMA domain, and OsHIPP19 and OsHIPP20 have

a CααX isoprenylation motif (-CSIM) at their C termini (Fig. 1).

Here, taking a biochemical and structural approach, we characterize the interaction between AVR-Pik and OsHIPP19. We demonstrate that AVR-PikD interacts with the HMA domain of OsHIPP19 with high affinity and that the interaction between AVR-PikD and the HMA domain of OsHIPP19 is tighter than the interactions between AVR-PikD and the integrated HMA domains of Pik-1 alleles. Further, we show that the tight interaction with OsHIPP19 is not unique to AVR-PikD, but is shared with other AVR-Pik variants. Finally, we present the crystal structure of AVR-PikF in complex with the HMA domain of OsHIPP19, revealing differences between the effector-binding surface of OsHIPP19 and that of the NLR protein Pikm-1. Our findings reveal the biochemical and structural basis of a *M. oryzae* effector protein's interaction with a putative virulence-associated host target and present opportunities for target-guided engineering of NLR IDs to extend their recognition profile.

Results

AVR-PikD binds to the HMA domain of OsHIPP19 with nanomolar affinity

In an independent study, four small HMA-domain-containing proteins were found to interact with AVR-PikD by yeast two-hybrid analysis (34). Of these, we selected OsHIPP19 for further study as it was identified most frequently in the initial yeast two-hybrid screen (34). Based on the well-characterized interaction of AVR-PikD with the HMA domain of Pik-1 (29, 41, 42), we hypothesized that AVR-PikD would interact with the HMA domain of OsHIPP19. We defined the HMA domain of OsHIPP19 (OsHIPP19-HMA hereafter) as amino acids 1 to 77 inclusive. This domain was expressed and purified from *Escherichia coli* (see Experimental procedures) and used in all subsequent work *in vitro*. Intact mass
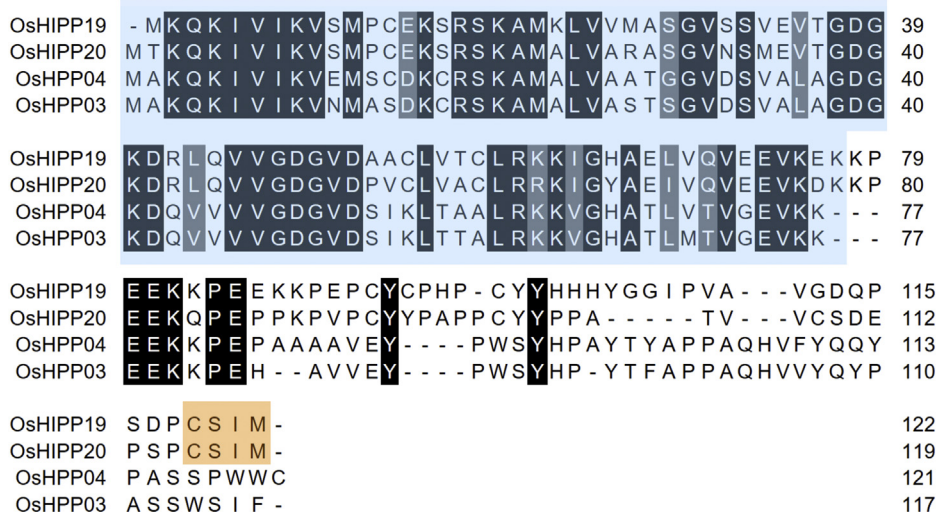

Figure 1. Amino acid sequence alignment of the AVR-PikD interactors identified by yeast two-hybrid (34)**, OsHIPP19 (LOC_Os04g39350), OsHIPP20 (LOC_Os04g39010), OsHPP03 (LOC_Os02g37290), and OsHPP04 (LOC_Os02g37300).** The alignment was produced with Clustal Omega and colored using BoxShade. The HMA domain is highlighted in *blue*, and the isoprenylation motif in OsHIPP19 and OsHIPP20 is highlighted in *orange*.
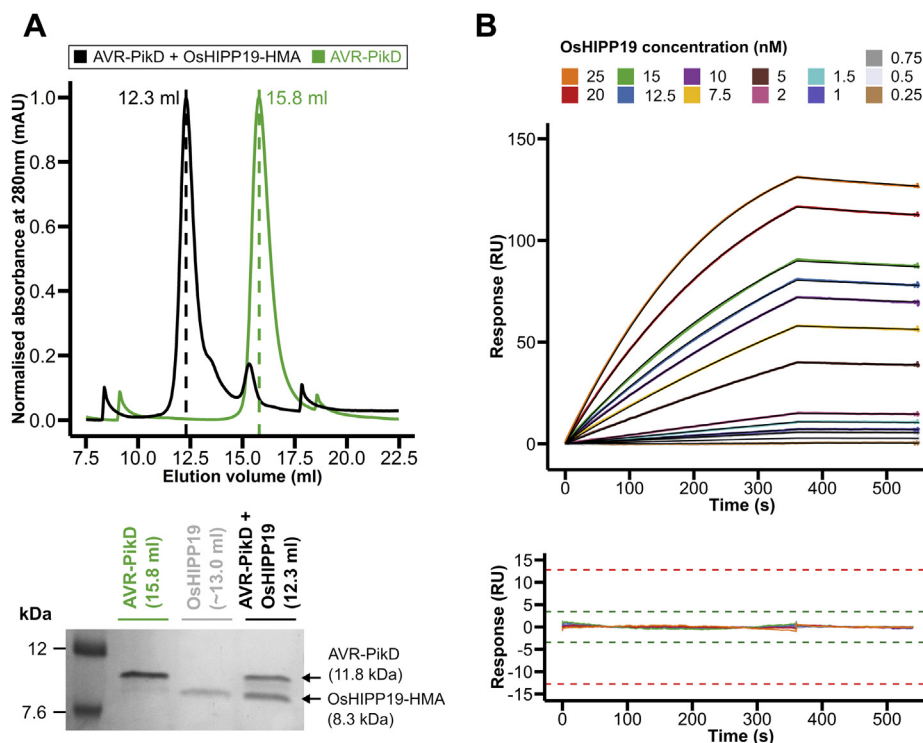
A

B

Figure 2. AVR-PikD interacts with the HMA domain of OsHIPP19 with nanomolar affinity *in vitro*. *A*, normalized analytical gel filtration traces for AVR-PikD alone (*green*) and AVR-PikD with OsHIPP19-HMA (*black*). The SDS-PAGE gel shows fractions from the peak elution volumes of each sample, demonstrating that AVR-PikD and OsHIPP19 coelute. OsHIPP19-HMA absorbs UV light at 280 nm very poorly (molar extinction coefficient of 360 cm^{-1}M^{-1}), so no peak is visible for OsHIPP19-HMA. *B*, multicycle kinetics data from surface plasmon resonance (*colored lines*) and 1-to-1 binding model fitted to the data (*black lines*) with the residuals plotted below. *Green* and *red* acceptance thresholds are determined by the Biacore T100 evaluation software.

spectrometry confirmed a molecular mass of 8323 Da for the purified protein, which exactly matched the theoretical mass.

First, we used analytical gel filtration to qualitatively test for interaction between AVR-PikD and OsHIPP19-HMA. When combined, the two proteins coeluted from the column, at an earlier elution volume than observed for either protein alone, demonstrating that AVR-PikD and OsHIPP19-HMA form a complex *in vitro* (Fig. 2A). The *Phytophthora infestans* effector PexRD54, which targets the autophagy-related protein ATG8 in its host (*Solanum tuberosum*) (43, 44), was used as a negative control and did not coelute with OsHIPP19-HMA, nor was a shift in elution volume observed for PexRD54 in the presence of OsHIPP19 (Fig. S1).

To investigate the affinity of the interaction between AVR-PikD and OsHIPP19-HMA, we used surface plasmon resonance (SPR). AVR-PikD was immobilized on a Ni^{2+}-NTA chip *via* a noncleavable 6xHis tag at the C terminus of the protein. OsHIPP19-HMA, at a range of concentrations between 0.25 nM and 25 nM, was flowed over the chip. A 1:1 binding model was used to fit the data (Fig. 2B) and to estimate the rate constants k_a and k_d for the interaction (Table S1), from which the equilibrium dissociation constant, K_D, could be calculated ($K_D = k_d/k_a$). The K_D value obtained from the data shown in Figure 2B was 0.7 nM. Two further replicates were performed with similar results (K_D = 0.6 nM and K_D = 0.9 nM). We conclude that AVR-PikD binds to OsHIPP19 with nanomolar affinity.

AVR-PikD binds to the HMA domain of OsHIPP19 with higher affinity than to the integrated HMA domains of Pikp-1 and Pikm-1

The HMA domain of OsHIPP19 shares 51% amino acid sequence identity with the integrated HMA domains of both Pikp-1 and Pikm-1 (Fig. 3, *A* and *B*). Previous work has shown that AVR-PikD binds to the integrated HMA domains of Pikp-1 and Pikm-1 with nanomolar affinity (29, 42). To compare the binding of AVR-PikD to the integrated HMA domains with its binding to OsHIPP19-HMA, we again used SPR. AVR-PikD was immobilized on a Ni^{2+}-NTA chip *via* a C-terminal 6xHis tag. Three different concentrations of each HMA domain (2 nM, 5 nM, and 20 nM) were flowed over the chip, and the binding (R_{obs}, measured in response units (RU)) was recorded. The R_{obs} for each HMA was then expressed as a percentage of the maximum theoretical response (R_{max}) that would be obtained if each immobilized molecule of AVR-PikD was bound to the HMA domain, referred to as %R_{max}. Mutating glutamate-230 of Pikp-HMA to arginine was predicted to disrupt the interaction of the HMA domain with AVR-PikD, and therefore Pikp^{E230R}-HMA was used as a negative control. Consistent with previous data, AVR-PikD interacted with the HMA domains of Pikp-1 and Pikm-1 with similar apparent affinity (Fig. 3C, Fig. S2). Interestingly, AVR-PikD bound to OsHIPP19-HMA with higher apparent affinity (larger %R_{max}) than to the HMA domains of either
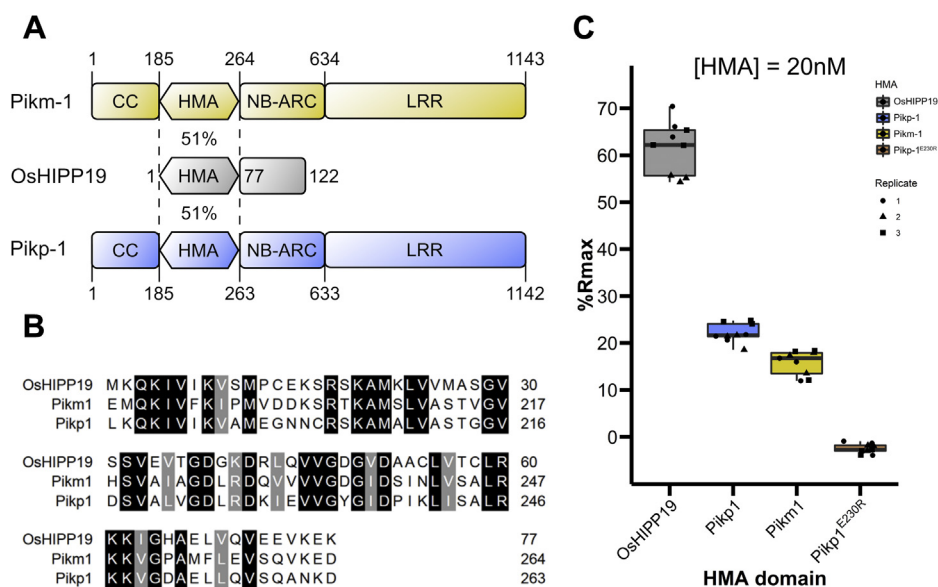
Figure 3. AVR-PikD interacts with the HMA domain of OsHIPP19 with higher affinity than with the integrated HMA domains of Pikp-1 or Pikm-1. *A,* schematic representation of Pikm-1, Pikp-1 and OsHIPP19. OsHIPP19-HMA shares 51% sequence identity with both Pikp-HMA and Pikm-HMA. *B,* amino acid sequence alignment of the HMA domains of OsHIPP19, Pikp-1, and Pikm-1. The alignment was produced with Clustal Omega and colored using BoxShade. *C, boxplots* showing the %Rmax observed for the interactions between AVR-PikD and each of the HMA domains. %Rmax is the percentage of the theoretical maximum response, assuming a 1:1 HMA:effector binding model for OsHIPP19-HMA and Pikm-HMA, and a 2:1 binding model for Pikp-HMA and Pikp^{E230R}-HMA. The center line of the box represents the median and the box limits are the *upper* and *lower quartiles*. The whiskers extend to the smallest value within $Q_1 - 1.5\times$ the interquartile range (IQR) and the largest value within $Q_3 + 1.5\times$ IQR. Individual data points are represented as black shapes. The experiment was repeated three times, with each experiment consisting of three technical replicates. Plots were produced using the ggplot2 package (71) in R (72).

Pikp-1 or Pikm-1 (Figure 3*C*, Fig. S2) at each of the three concentrations tested.

Additional AVR-Pik variants interact with the HMA domain of OsHIPP19

The five AVR-Pik variants A, C, D, E, and F differ in only five amino acid positions (Fig. S3). Previous work has shown that only a subset of AVR-Pik variants interact with the HMA domains of Pikp-1 and Pikm-1 (29, 42). Notably, neither AVR-PikC nor AVR-PikF interacts with the HMA domains of Pikp-1 and Pikm-1, and therefore neither variant triggers Pik-mediated immunity in plants. We hypothesized that AVR-PikC and AVR-PikF may have evolved to avoid detection by the plant immune system, but still interact with their host target (OsHIPP19) to execute their virulence function.

To test this hypothesis, we used analytical gel filtration to qualitatively assess whether each of the AVR-Pik variants forms a complex with OsHIPP19 *in vitro*. We found that each of the AVR-Pik variants, including AVR-PikC and AVR-PikF, formed a complex with OsHIPP19-HMA (Fig. 4, Fig. S4). To investigate whether the amino acid polymorphisms between the different AVR-Pik variants influence their affinity for OsHIPP19, we determined the equilibrium dissociation constants for the interactions between OsHIPP19-HMA and AVR-PikC/AVR-PikF by SPR, as described earlier for AVR-PikD. The K_D values obtained for these interactions over three replicates were within a similar nanomolar range (1.1–1.9 nM for AVR-PikC and 0.8–1.0 nM for AVR-PikF) (Fig. 5, *A* and *B*, Table S1), indicating that AVR-PikC and

AVR-PikF also bind OsHIPP19 with similar nanomolar affinity.

Crystal structure of AVR-PikF in complex with OsHIPP19

Next, we defined the structural basis of interaction between OsHIPP19 and AVR-Pik effectors. As AVR-PikC and AVR-PikF do not bind any of the integrated HMA domains identified to date, their interaction with the HMA domain of OsHIPP19 was of particular interest. Both AVR-PikC and AVR-PikF were each coexpressed with OsHIPP19-HMA in *E. coli* and purified (see Experimental procedures for full details). Crystals of the complex between OsHIPP19-HMA and AVR-PikF were obtained in several conditions in the commercial Morpheus screen (Molecular Dimensions). The OsHIPP19-HMA/AVR-PikC complex did not crystallize in any of the commercial screens trialled. We therefore focused on OsHIPP19-HMA/AVR-PikF. Having confirmed the presence of both proteins in the purified complex by intact mass spectrometry (peaks in the spectrum at 8323 Da and 10,839 Da exactly matched the theoretical masses for OsHIPP19 and AVR-PikF (after subtracting 2 Da for the presence of an expected disulphide bond), respectively), we then obtained X-ray diffraction data to 1.9 Å resolution. The structure of the OsHIPP19-HMA/AVR-PikF complex was solved by molecular replacement (see Experimental procedures), using the crystal structure of a monomer of Pikp-HMA/AVR-PikD (PDB accession no. 5A6W) as a model. X-ray data collection, refinement, and validation statistics are shown in Table 1.
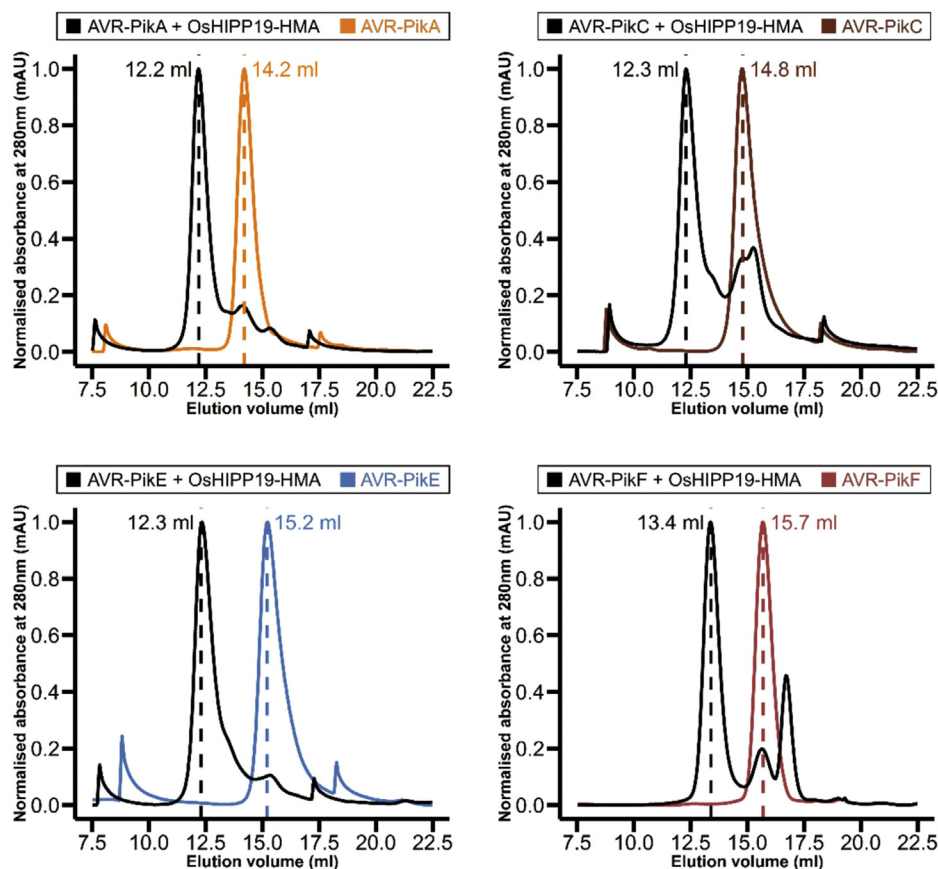
Figure 4. All AVR-Pik alleles interact with the HMA domain of OsHIPP19. Normalized analytical gel filtration traces for each effector allele alone (*colored*) and with OsHIPP19-HMA (*black*). The peak shift observed when each effector is combined with OsHIPP19-HMA indicates complex formation. OsHIPP19-HMA absorbs UV light at 280 nm very poorly (molar extinction coefficient of 360 cm^{-1}M^{-1}), so no peak is visible for OsHIPP19-HMA.

As anticipated, the HMA domain of OsHIPP19 adopts the well-characterized HMA fold (Pfam: PF00403) consisting of a four-stranded antiparallel β-sheet and two α-helices arranged in an α-β sandwich. The loop between β1 and α1 containing the degenerate metal-binding motif (MPCEKS) is poorly defined in the electron density, and OsHIPP19$^{Glu14-Lys15}$ could not be positioned.

Overall, the structure of AVR-PikF is very similar to previously determined structures of other AVR-Pik variants and comprises a core six-stranded β-sandwich, conserved among the MAX effectors (45), with an N-terminal extension (AVR-PikF$^{Arg31-Pro52}$). A disulfide bond between AVR-PikF^{Cys54} and AVR-PikF^{Cys70} stabilizes the β-sandwich structure.

OsHIPP19-HMA and AVR-PikF form a 1:1 complex. The position of AVR-PikF relative to the HMA domain of OsHIPP19 is similar to the previously determined structures of AVR-Pik effectors in complex with integrated Pik-HMA domains (Fig. 6) (29, 42). AVR-PikF only differs from AVR-PikA by a single polymorphism at position 78, and the structures of the OsHIPP19-HMA/AVR-PikF complex and Pikm-HMA/AVR-PikA complex are similar. The RMSD, as calculated in Coot (46) using secondary structure matching, between HMA domains is 0.826 Å using 74 residues. The RMSD between the AVR-Pik effectors is 0.437 Å using 81 residues. The overall RMSD between the two complexes is 0.71 Å using 155 residues.

The interface between OsHIPP19-HMA and AVR-PikF is extensive, burying 23.1% and 19.5% of the total accessible surface area of the HMA domain (1068.5 Å^2) and effector (1022.0 Å^2), respectively. The total interface area (sum of the buried surface area of each component divided by 2) for the OsHIPP19-HMA/AVR-PikF complex is 1045.3 Å^2, larger than the total interface area of the Pikm-HMA/AVR-PikA complex (918.3 Å^2) (42), and indeed any of the Pik-HMA/AVR-Pik complexes determined to date. Interface analysis parameters determined by QtPISA are shown in Table S2.

Differences over three interfaces, but particularly at interface 3, underpin the higher affinity of OsHIPP19 for AVR-Pik relative to the integrated Pikm-1 HMA domain

Previous analysis of the interface between AVR-PikA and Pikm-HMA revealed three main regions, numbered 1 to 3, which contribute to the interaction between the two proteins. Similarly, three distinct regions can be identified in the complex of OsHIPP19-HMA/AVR-PikF. Differences between OsHIPP19-HMA and Pikm-HMA at each of these three interfaces may contribute to the differences in specificity and affinity of the interactions between the HMA domains and AVR-Pik variants.
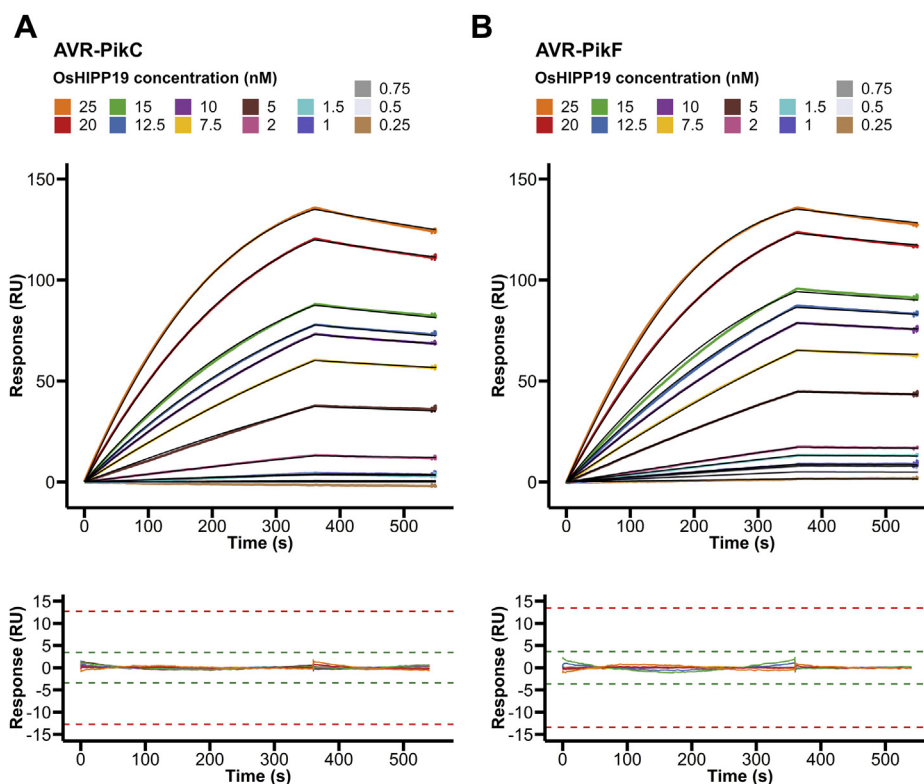
Figure 5. AVR-PikC and AVR-PikF interact with the HMA domain of OsHIPP19-HMA with nanomolar affinity. Multicycle kinetics data from surface plasmon resonance experiments for the interaction between OsHIPP19-HMA and *A*) AVR-PikC or *B*) AVR-PikF. Experimental data is shown as colored lines, and 1-to-1 binding model fitted to the data overlaid (*black lines*). The residuals are plotted below; *green* and *red* acceptance thresholds are determined by the Biacore T100 evaluation software.

Interface 1 of AVR-PikA/Pikm was characterized by a weak (3.5 Å) hydrogen bond between the side chain of $Pikm^{Lys191}$ and the main-chain carbonyl group of $AVR-PikA^{Thr69}$ and a hydrophobic interface contributed by $Pikm^{Met189}$ (42). In the AVR-PikF/OsHIPP19 complex, the hydrophobic interface is absent; however, the lysine residue is conserved and forms a second hydrogen bond (2.9 Å) with the side chain of $AVR-PikF^{Thr69}$ (Fig. 6).

In both complexes, interface 2 involves residues from β2 and β3 of the HMA domain ($Pikm^{Ser219-Val233}$ and $OsHIPP19^{Ser31-Val46}$), which interact with residues in β2 and the N-terminal extension of AVR-PikF (including the polymorphic residues 46, 47, and 48). AVR-PikA and AVR-PikF share the asparagine-alanine-aspartate (NAD) triad in the polymorphic positions 46, 47, and 48. The interactions between these residues and residues in β2 and β3 of the HMA domain underpin the differential recognition of AVR-PikD, AVR-PikE, and AVR-PikA by Pikm (42). The side chain of $AVR-PikA^{Asn46}$ forms a single hydrogen bond with $Pikm^{Ser219}$. By contrast, the side chain of $AVR-PikF^{Asn46}$ is rotated and forms two hydrogen bonds with the side chains of $OsHIPP19^{Ser32}$ and $OsHIPP19^{Gln44}$ (Fig. 7*A*). Also located to interface 2, $AVR-PikF^{Asp66}$ forms hydrogen bonds with the main-chain amide group of $OsHIPP19^{Asp38}$ and side chain of $OsHIPP19^{Arg42}$, differing from the AVR-PikA/Pikm structure where a single hydrogen bond is formed between $AVR-PikA^{Asp66}$ and $Pikm^{Lys195}$. The side chain of $Pikm^{Asp225}$ forms two hydrogen bonds

with the side chain of $AVR-PikA^{Arg64}$; the aspartate is conserved in OsHIPP19 ($OsHIPP19^{Asp38}$) and forms similar interactions with $AVR-PikF^{Arg64}$ (Fig. 6).

Interface 3 comprises residues from β4 of the HMA domain extending to the C terminus of the protein ($Pikm^{Met254-Asp264}$ and $OsHIPP19^{Glu67-Glu76}$). In the complex between Pikm-HMA/AVR-PikA, this interface is defined by main-chain hydrogen bonding between β4 of the HMA domain and β3 of AVR-PikA and, notably, the positioning of $Pikm^{Lys272}$ into a pocket on the surface of the effector. The conserved $OsHIPP19^{Lys75}$ binds into a similar pocket on the surface of AVR-PikF, formed by $AVR-PikF^{Glu53}$, $AVR-PikF^{Tyr71}$, $AVR-PikF^{Ser72}$, and $AVR-PikF^{Trp74}$. In addition to main-chain hydrogen bonding between β4 of OsHIPP19-HMA and β3 of AVR-PikF, additional hydrogen bonds are contributed by $OsHIPP19^{Glu72}$ and $OsHIPP19^{Glu73}$. Strikingly, the side chain of $OsHIPP19^{Glu72}$ (a serine in the corresponding position in Pikm-HMA) forms a hydrogen bond (2.8 Å) with the main-chain amide group of $AVR-PikF^{Tyr71}$ (Fig. 7*B*). In addition, the side chain of $OsHIPP19^{Glu73}$ (a glutamine in the corresponding position in Pikm-HMA) forms a salt bridge interaction with the side chain of $AVR-PikF^{Lys75}$. Overall, hydrogen bonding between the HMA domain and the effector at interface 3 is more extensive in the OsHIPP19-HMA/AVR-PikF complex than in the Pikm-HMA/AVR-PikA complex, which likely contributes to the difference in binding affinity.

Table 1
Data collection and refinement statistics for the AVR-PikF/OsHIPP19-HMA complex

Data collection statistics	
Wavelength (Å)	0.976
Space group	P $2_1 2_1 2_1$
Cell dimensions a, b, c (Å)	29.78, 53.78, 98.03
Resolution (Å)[a]	98.03–1.90 (1.94–1.90)
R_{merge} (%)	12.9 (112.9)
$I/\sigma I$	12.4 (1.9)
Completeness (%)	100 (100)
Unique reflections	13,077 (811)
Redundancy	12.6 (11.1)
CC(1/2) (%)	99.9 (91.0)
Refinement and model statistics	
Resolution (Å)[a]	98.03–1.90 (1.95–1.90)
R_{work}/R_{free} (%)	19.6/23.3 (27.5/27.1)
No. atoms	
Protein	2416
Water	67
B-factors	
Protein	38.1
Water	37.4
R.m.s deviations	
Bond lengths (Å)	0.015
Bond angles (°)	1.661
Ramachandran plot (%)[b]	
Favored	98.0
Allowed	2.0
Outliers	0
MolProbity score	1.39 (98th percentile)

[a] The highest resolution shell is shown in parentheses.
[b] As calculated by MolProbity.

Polymorphic residue AVR-PikF[Lys78] is located at the binding interface with OsHIPP19

The single difference between AVR-PikA, which binds to Pikm-1 to trigger plant immunity, and AVR-PikF, which does not, is the residue at position 78 (methionine in AVR-PikA and lysine in AVR-PikF). The polymorphic AVR-PikF[Lys78] is positioned at the binding interface with OsHIPP19 and is well defined in the electron density. Interestingly, the side chain of

the lysine adopts an unusual conformation (determined by MolProbity with reference to lysine side chains in deposited structures in the protein data bank) (Fig. S5). We suggest that while this residue is sufficient to disrupt the interaction between the integrated HMA domains and AVR-PikF, increased intermolecular interactions between OsHIPP19 and AVR-PikF, as described earlier, compensate for the disruptive influence of AVR-PikF[Lys78] and maintain the interaction between the two proteins.

Discussion

Recognition of the *M. oryzae* effector AVR-Pik is mediated by the paired rice NLR proteins Pik-1/Pik-2. AVR-Pik directly interacts with an integrated HMA domain in Pik-1. However, the stealthy variants AVR-PikC and AVR-PikF avoid binding to the integrated Pik-1 HMA domain and evade plant defenses. Here we show that all AVR-Pik variants, including AVR-PikC and AVR-PikF, interact with the HMA domain of rice HMA isoprenylated plant protein 19 (OsHIPP19), a putative virulence target, with nanomolar affinity (Fig. 8). We observe that AVR-Pik variants interact with OsHIPP19-HMA with higher apparent affinity than with the integrated Pik-HMA domains. By solving the crystal structure of AVR-PikF bound to OsHIPP19-HMA and comparing it with the previously published structures of AVR-Pik effectors bound to Pikp-HMA or Pikm-HMA, we identify differences in the binding interfaces that underpin the increased affinity and broader specificity of the OsHIPP19-HMA/AVR-Pik interaction.

AVR-Pik binds OsHIPP19-HMA with higher affinity than integrated Pik-1 HMA domains

The identification of diverse protein domains integrated into the core structure of NLRs has provided new insights into the molecular mechanisms by which NLR proteins
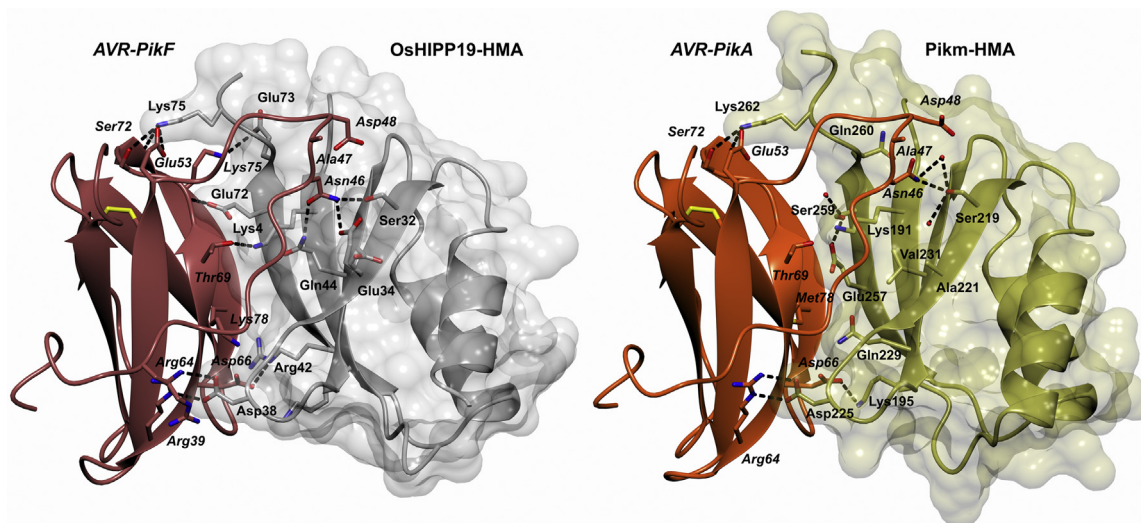

Figure 6. Comparison of the crystal structure of AVR-PikF in complex with the HMA domain of OsHIPP19 (7B1I) with the previously published crystal structure of AVR-PikA in complex with the HMA domain of Pikm-1 (6FUD, (42)). The structures of AVR-PikF and OsHIPP19-HMA are represented as *red* and *gray* ribbons, respectively, with the molecular surface of OsHIPP19-HMA also shown. The structures of AVR-PikA and Pikm-HMA are represented as *orange* and *gold* ribbons, respectively, with the molecular surface of Pikm-HMA also shown. The side chains of amino acids of interest are displayed as *cylinders*. Hydrogen bonds are represented by *dashed lines*.
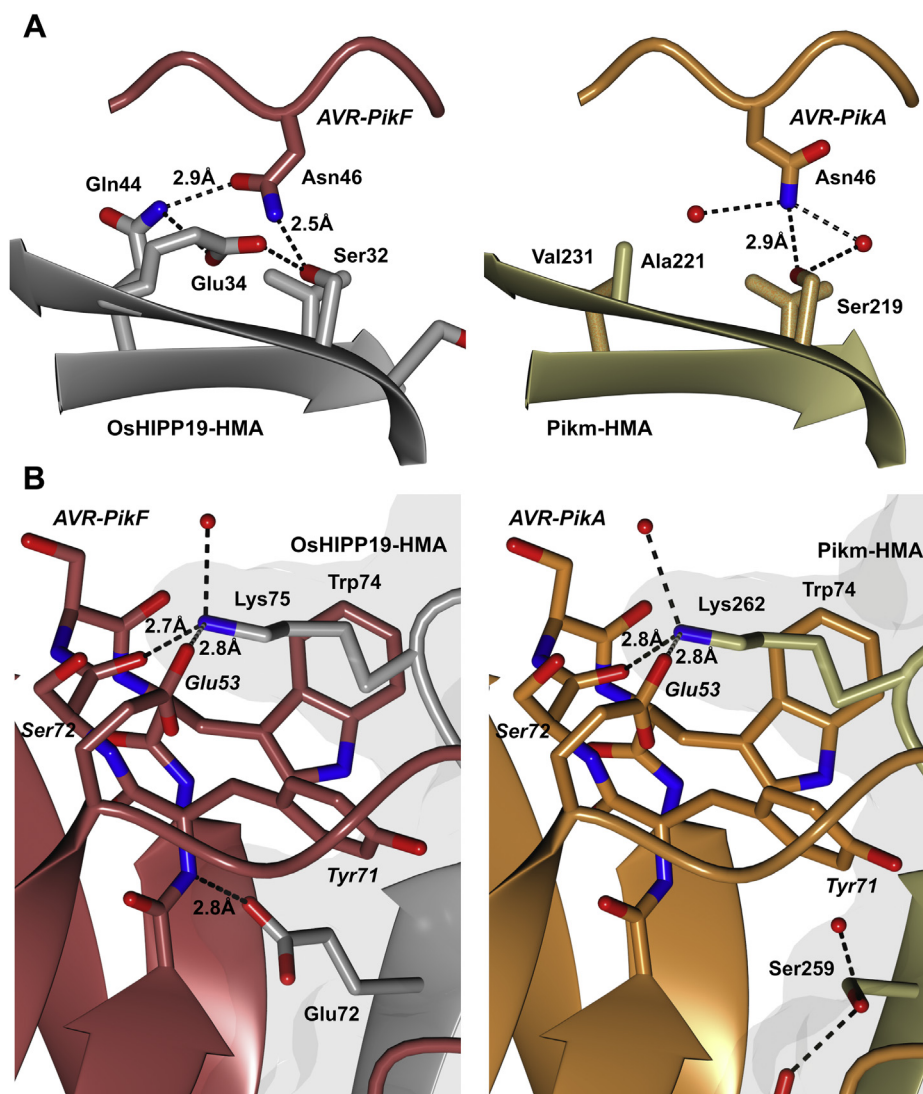
Figure 7. Comparison of the binding interfaces in the crystal structure of AVR-PikF in complex with the HMA domain of OsHIPP19 (7B1I) with the previously published crystal structure of AVR-PikA in complex with the HMA domain of Pikm-1 (6FUD, (42)). The structures of AVR-PikF and OsHIPP19-HMA are represented as *red* and *gray ribbons*, respectively, with the molecular surface of OsHIPP19-HMA also shown. The structures of AVR-PikA and Pikm-HMA are represented as *orange* and *gold ribbons*, respectively, with the molecular surface of Pikm-HMA also shown. The side chains of amino acids of interest are displayed as *cylinders*. Hydrogen bonds are represented by *dashed lines*. *A*, AVR-PikF[Asn46] is rotated and forms an additional hydrogen bond with OsHIPP19-HMA compared with AVR-PikA[Asn46] bound to Pikm-HMA. The side chain of OsHIPP19[Glu34] exists in two alternate conformations, both supported by the electron density. For clarity, only the relevant conformation is shown here. *B*, OsHIPP19[Glu72] forms an additional hydrogen bond with the main chain of AVR-PikF.

detect the presence of effectors. However, little is known about how effectors interact with host virulence-associated targets that are related to these IDs. Direct binding of AVR-Pik to the integrated HMA domain of Pik-1 is necessary for activation of immunity by the cooperative NLR proteins Pik-1 and Pik-2. Similarly, the rice NLR pair Pia (also known as RGA5/RGA4) detects the presence of AVR-Pia or AVR1-CO39 *via* a direct interaction between the effector and the HMA domain at the C terminus of the Pia sensor NLR (RGA5) (22, 33, 47). The ID hypothesis proposes that these domains have their origins in the host virulence targets of the effector (25). As effector binding triggers immune signaling, we might expect the integrated HMA domains of Pikp-1 and Pikm-1 to bind the effector more tightly than the HMA

domain of the putative virulence target OsHIPP19, as their only expected function is to bait the effector. Somewhat surprisingly, our results show that AVR-PikD interacts with OsHIPP19-HMA with higher affinity than Pikp-HMA or Pikm-HMA.

It is important to note that the HMA domains are being studied in isolation, without the biological context of the full-length protein. Other Pik-1 domains may provide additional contacts with the effector, which increase the affinity of the receptor for AVR-PikD. Furthermore, the molecular details of the mechanism by which Pik-1 and Pik-2 cooperate to initiate immune signaling remain unknown; Pik-2 may also influence the affinity of the interaction between AVR-PikD and Pik-1.
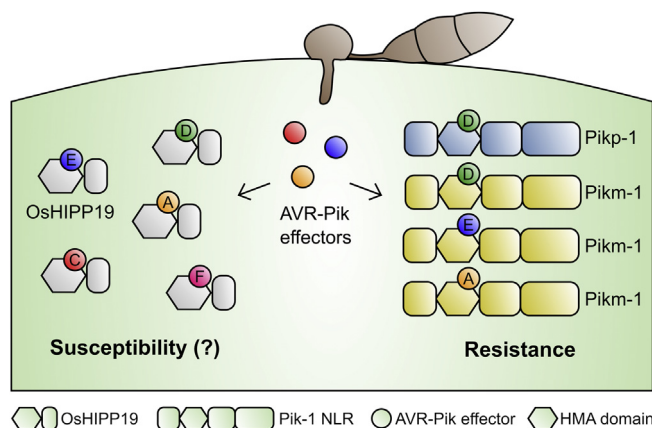
Figure 8. Schematic representation of the interactions between AVR-Pik effector alleles and the HMA domains of OsHIPP19 and Pik-1 NLR proteins.

HIPPs and HPPs may be plant immunity hubs and are targeted by multiple pathogen proteins

Although AVR-PikD interacts with Pikp-HMA and Pikm-HMA with lower apparent affinity than with OsHIPP19-HMA, the affinity of the interaction is sufficient to trigger immune signaling and disease resistance. Therefore, higher-affinity binding of the integrated HMA domain to the effector may not provide any additional evolutionary benefit. Furthermore, it is has been suggested that AVR-Pia and AVR1-CO39 may also interact with rice HMA domain-containing proteins (33). Studies of the interactomes of effectors from different phytopathogens have identified common host targets, proposed to be immunity-related "hubs," which are targeted by diverse pathogens to achieve infection (48). The movement protein of potato mop top virus interacts with NbHIPP26 to promote long-distance viral movement (49), and AtHIPP27 is reported to be a susceptibility factor for infection by the beet cyst nematode *Heterodera schachtii* (50). There may be more as-yet unidentified effectors, produced by diverse pathogens, which target HIPPs or HPPs to promote infection. It is also tempting to speculate that the Pik-1/Pik-2 NLR pair may recognize effectors outside the AVR-Pik allelic series, trading high-affinity binding to AVR-Pik for binding to other effectors. The NLR pair RRS1/RPS4 recognizes the structurally diverse effectors AvrRps4 from *Pseudomonas syringae pv. pisi* and PopP2 from *Ralstonia solanacearum via* an integrated WRKY domain at the C terminus of RRS1 (51–53), highlighting how the incorporation of a domain targeted by multiple effectors into an NLR can lead to immunity to diverse pathogens.

AVR-Pik binds to OsHIPP19-HMA *via a similar interface to the integrated HMA domain of Pik-1*

As the integrated domain hypothesis proposes that these domains have their origins in the host virulence targets of the effector, it would be expected that the effector binds in a similar manner to both its virulence target and the ID of the NLR protein. Consistent with this, we observe that the overall

binding interface between AVR-PikF and the HMA domain of OsHIPP19 is very similar to that between AVR-Pik and the integrated HMA domains of Pikp-1 and Pikm-1 (RMSD for the complex is 0.71 Å using 155 amino acids). We hypothesize that other effector/NLR-ID interfaces would likewise mimic the interface between the effector and its host target.

The stealthy effector variants AVR-PikC and AVR-PikF bind to OsHIPP19-HMA, but not to Pik-1 HMA domains

The Ala67Asp mutation that distinguishes AVR-PikC from AVR-PikE and the Met78Lys mutation that distinguishes AVR-PikF from AVR-PikA are both located at the interface of the effector with the HMA domain (37, 38). These mutations appear to be adaptive (37, 38, 42) and sufficient to prevent interaction with the integrated HMA domains of the various Pik-1 alleles. Here we show that these mutations do not preclude interaction between the effector and the HMA domain of OsHIPP19. The crystal structure of the complex between OsHIPP19/AVR-PikF reveals that the side chain of AVR-PikF^{Lys78} adopts an unusual conformation, likely imposed by a steric clash of more favorable conformations with OsHIPP19-HMA. This suggests that the OsHIPP19/AVR-PikF interaction is maintained by additional intermolecular contacts between the proteins, particularly at interface 3, rather than compensatory mutations in the HMA domain to accommodate the AVR-PikF^{Lys78} side chain. AVR-PikC contains an aspartate in position 67, but is otherwise identical to AVR-PikE, which has alanine in this position. We have previously shown that the side chain of AVR-PikC^{Asp67} disrupts hydrogen bonding between the effector and the HMA domain at interface 2 (38). Pikp-HMA does not interact with AVR-PikC; however, Pikh-HMA, which differs in a single amino acid at interface 3, is able to interact with this effector variant (38). This further demonstrates that unfavorable interactions can be overcome by compensatory mutations at other interfaces. This has broad implications for engineering protein–protein interactions, highlighting that compensatory mutations need not be physically located next to unfavorable amino acids.

Aside from integrated domains, other NLR regions, particularly LRR domains, can directly interact with pathogen effectors (54). In these cases, it is unlikely that the interface between the NLR and effectors directly mimics the interaction with virulence-associated targets. This has implications for the evolution of recognition. It suggests that effectors can escape recognition *via* mutation at one interface without impacting the effector's virulence-associated activity. Recognition *via* IDs may be more robust, as mutation in an effector that prevents recognition may also reduce the protein's disease-promoting activity. However, as is exemplified by the AVR-PikC and AVR-PikF effector variants, it can still be overcome without compromising the interaction between the effector and its target. Engineering IDs to more closely resemble the host target of an effector may provide more durable resistance, particularly where the virulence function of the effector is necessary for disease.

Future opportunities for engineering integrated domains to extend the recognition capabilities of NLRs

The emergence of an allelic series of AVR-Pik effectors may have been driven by the deployment of rice varieties carrying Pik-1 alleles in agriculture (55–57). AVR-PikC and AVR-PikF avoid binding to the integrated HMA domain of Pik-1, and *M. oryzae* isolates carrying AVR-PikC and AVR-PikF are virulent on Pik-containing rice lines. The spread of isolates containing these novel variants represents a threat to global rice production (37). Understanding the interaction between AVR-PikF and the HMA domain of OsHIPP19 will guide future efforts to engineer a Pik-1 receptor with an HMA domain resembling that of OsHIPP19, to which these stealthy variants bind. Such a variant may be capable of delivering disease resistance to *M. oryzae* strains carrying AVR-PikC and AVR-PikF.

Experimental procedures

Protein production and purification

AVR-Pik effector proteins were produced with a cleavable N_t SUMO tag and a noncleavable C_t His tag from pOPIN-E (58) in *E. coli* SHuffle (59) and purified as previously described (29). HMA domains were produced with a cleavable

$$R_{max}\ (RU) = \frac{M_W\ (analyte)}{M_W\ (ligand)} \times stoichiometry \times ligand\ capture\ (RU)$$

N_t His-MBP tag from pOPIN-M in *E. coli* SHuffle. Pikp-HMA and Pikm-HMA were produced and purified as previously described (29). For production of OsHIPP19-HMA, inoculated 1 l cell cultures were grown in autoinduction media (60) at 30 °C. One millimolar TCEP was included in the buffer for the final gel filtration of OsHIPP19-HMA. Protein concentration was determined using a Direct Detect Infrared Spectrometer (Millipore Sigma).

Analytical gel filtration

Experiments were conducted at 4 °C using a Superdex 75 10/300 GL column (GE Healthcare) equilibrated in running buffer (20 mM HEPES pH 7.5, 150 mM NaCl, 1 mM TCEP). To investigate whether the effector and OsHIPP19-HMA form a complex, the two proteins were combined in a 1:1 M ratio and incubated on ice for 1 h prior to analysis. Each protein was also analyzed alone, at a concentration equivalent to that present in the complex. For each experiment, 100 μl protein was injected at a flow rate of 0.5 ml/min, and 500 μl fractions were collected for analysis by SDS-PAGE. The extinction coefficient of OsHIPP19-HMA is so low that there is no peak distinguishable from background noise for OsHIPP19-HMA on its own. The elution volume reported is an estimate based on the SDS-PAGE gel. Analytical gel filtration experiments with AVR-PikA, AVR-PikC, AVR-PikD, and AVR-PikE were performed using a different system to experiments with AVR-PikF and PexRD54. The traces from experiments with

AVR-PikA, AVR-PikC, AVR-PikD, and AVR-PikE contain regular spikes in the UV trace, which are caused by a mechanical issue with this FPLC system. These spikes occurred at regular intervals, regardless of whether a protein had been injected or buffer alone was flowing through the system and/or column.

Surface plasmon resonance

SPR was carried out using a Biacore T100 (GE Healthcare) at 25 °C and at a flow rate of 30 μl/min. The running buffer was 20 mM HEPES pH 7.5, 860 mM NaCl, and 0.1% (v/v) Tween20. Flow cell (FC) 2 of an NTA chip (GE Healthcare) was activated with 30 μl 0.5 mM $NiCl_2$. In total, 30 μl of the 6xHis-tagged effector (the ligand) was immobilized on FC2 to give a response between 200 and 400 RU. The HMA domain (the analyte) was then flowed over both FC1 and FC2 for 360 s, followed by a dissociation time of 180 s. The NTA chip was regenerated after each cycle with 30 μl 0.35 M EDTA pH 8.0.

The background response from FC1 (nonspecific binding of the HMA domain to the chip) was subtracted from the response from FC2. For %R_{max} experiments, the binding response (R_{obs}) was measured immediately prior to the end of injection and expressed as a percentage of the theoretical maximum response (R_{max}), calculated as follows:

A 1:1 HMA:effector binding model for OsHIPP19-HMA and Pikm-HMA, and a 2:1 HMA:effector binding model for Pikp-HMA and Pikp^{E230R}-HMA, was used based on whether the respective HMA domain is a monomer or a dimer in solution (supported by previously determined crystal structures (29, 42)).

For kinetics analysis, a 1:1 binding model was applied to the data. The R_{max} was fitted locally to reflect the regeneration of the chip and subsequent recapture of Ni^{2+} and effector between cycles. The resulting estimates for the k_a and k_d values were used to calculate the reported K_D.

$$K_D\ (M) = \frac{k_d\ (s^{-1})}{k_a\ (M^{-1}s^{-1})}$$

Copurification and crystallization of OsHIPP19-HMA/AVR-PikF

MBP-OsHIPP19-HMA (pOPIN-A) and 6xHis-SUMO-AVR-PikF (pOPIN-S3C) were coexpressed in *E. coli* SHuffle cells. In total, 8 × 1 l of cell culture was grown in autoinduction media, containing carbenicillin and kanamycin (final concentration of 100 μg/ml and 30 μg/ml, respectively) to select for the plasmids, at 30 °C for 20 h. Cells were pelleted by centrifugation (5663*g* for 7 min at 4 °C) and resuspended in lysis buffer (50 mM Tris-HCl pH 8.0, 50 mM glycine, 0.5 M NaCl, 20 mM imidazole, 5% (v/v) glycerol, 1 cOmplete EDTA-free protease inhibitor cocktail tablet (Roche) per 50 ml

buffer). Resuspended cells were lysed by sonication with a VibraCell sonicator (SONICS), and whole-cell lysate was clarified by centrifugation at 38,724g for 30 min at 4 °C. An AKTA Xpress (GE Healthcare) system was used to carry out a two-step purification at 4 °C. The clarified cell lysate was first injected onto a 5 ml Ni^{2+}-NTA column (GE Healthcare). The MBP-OsHIPP19-HMA/6xHis-SUMO-AVR-PikF complex was step-eluted with elution buffer (50 mM Tris-HCl pH 8.0, 50 mM glycine, 0.5 M NaCl, 500 mM imidazole, 5% (v/v) glycerol), and applied to a Superdex 75 26/600 gel filtration column equilibrated in running buffer (20 mM HEPES pH 7.5 and 150 mM NaCl). MBP and 6xHis-SUMO tags were cleaved by incubation with 3C protease (1 μg protease per mg of fusion protein) at 4 °C overnight and removed by passing the sample through a 5 ml Ni^{2+}-NTA column connected to a 5 ml dextrin sepharose (MBPTrap) column (GE Healthcare), both equilibrated in lysis buffer. Fractions containing the OsHIPP19-HMA/AVR-PikF complex were concentrated and injected onto a Superdex 75 26/600 column equilibrated in running buffer +1 mM TCEP. Protein concentration was determined using a Direct Detect Infrared Spectrometer (Millipore Sigma).

Crystallization trials were set up in 96-well plates using an Oryx Nano robot (Douglas Instruments). In total, 0.3 μl of 11 mg/ml protein was combined with 0.3 μl reservoir solution from the commercial Morpheus screen (Molecular Dimensions). Crystals appeared in several conditions. For X-ray diffraction, a crystal from condition D9 (0.12 M Alcohols [0.2 M 1,6-Hexanediol; 0.2 M 1-Butanol; 0.2 M 1,2-Propanediol; 0.2 M 2-Propanol; 0.2 M 1,4-Butanediol; 0.2 M 1,3-Propanediol], 0.1 M Buffer System 3 pH 8.5 [1 M Tris (base); BICINE], 50% v/v Precipitant Mix 1 [40% v/v PEG 500* MME; 20% w/v PEG 20000]) was cryoprotected in mother liquor, mounted in a loop, and frozen in liquid nitrogen.

Data collection and model refinement

X-ray diffraction data were collected on beamline i03 at the Diamond Light Source. 3600 images were collected with an exposure time of 0.01 s and oscillation of 0.1°. The diffraction images were indexed and scaled using the autoPROC pipeline (61). The scaled but unmerged data file was passed to AIMLESS (62) for data reduction. The structure was solved by molecular replacement, carried out with PHASER (63) using a monomer of Pikp-HMA in complex with AVR-PikD (PDB accession: 5A6W) as a model. OsHIPP19-HMA and AVR-PikF were built into the data using BUCCANEER (64). Iterative cycles of manual adjustment, refinement, and validation were carried out using COOT (46) and REFMAC (65) through CCP4i2 (66). Final validation was performed by MolProbity (67). qtPISA (68) was used for interface analysis. Structure figures were produced using the CCP4mg molecular graphics software (69).

Data availability

The protein structure of the complex between OsHIPP19-HMA and AVR-PikF and the data used to derive this have been deposited at the PDB with accession number 7B1I.

Author contributions—J. H. R. M. Conceptualization, Data Curation, Formal Analysis, Investigation, Methodology, Validation, Visualization, Writing—Original Draft, Writing—Review and Editing; M. F. Formal Analysis, Investigation, Methodology, Supervision, Validation, Writing—Review and Editing; A. M. Investigation, Supervision, Writing—Review and Editing; H. S. Investigation, Writing—Review and Editing; C. J. Investigation, Writing—Review and Editing; R. T. Conceptualization, Funding Acquisition, Project Administration, Writing—Review and Editing; S. K. Conceptualization, Supervision, Funding Acquisition, Writing—Review and Editing; M. J. B. Conceptualization, Funding Acquisition, Project Administration, Resources, Supervision, Validation, Writing—Original Draft, Writing—Review and Editing.

References

1. Wilson, R. A., and Talbot, N. J. (2009) Under pressure: Investigating the biology of plant infection by *Magnaporthe oryzae*. *Nat. Rev. Microbiol.* **7**, 185–195
2. Dean, R., Van Kan, J. A. L., Pretorius, Z. A., Hammond-Kosack, K. E., Di Pietro, A., Spanu, P. D., Rudd, J. J., Dickman, M., Kahmann, R., Ellis, J., and Foster, G. D. (2012) The top 10 fungal pathogens in molecular plant pathology. *Mol. Plant Pathol.* **13**, 414–430
3. Wang, X., Lee, S., Wang, J., Ma, J., Bianco, T., and Ji, Y. (2014) Current advances on genetic resistance to rice blast disease. In: Yan, W., Bao, J., eds. *Rice - Germplasm, Genetics and Improvement,* IntechOpen, London, UK: 195–217
4. Pennisi, E. (2010) Armed and dangerous. *Science* **327**, 804–805
5. Kato, H., Yamamoto, M., and Yamaguchi-Ozaki, T. (2000) Pathogenicity, mating ability and DNA restriction fragment length polymorphisms of *Pyricularia* populations isolated from Gramineae, Bambusideae and Zingiberaceae plants. *J. Gen. Plant Pathol.* **66**, 30–47
6. Yoshida, K., Saunders, D. G., Mitsuoka, C., Natsume, S., Kosugi, S., Saitoh, H., Inoue, Y., Chuma, I., Tosa, Y., Cano, L. M., Kamoun, S., and Terauchi, R. (2016) Host specialization of the blast fungus *Magnaporthe*

oryzae is associated with dynamic gain and loss of genes linked to transposable elements. *BMC Genomics* **18**, 370

7. Petit-Houdenot, Y., Langner, T., Harant, A., Win, J., and Kamoun, S. (2020) A clone resource of *Magnaporthe oryzae* effectors that share sequence and structural similarities across host-specific lineages. *Mol. Plant Microbe Interact.* **33**, 1032–1035

8. Park, C.-H., Chen, S., Shirsekar, G., Zhou, B., Khang, C. H., Songkumarn, P., Afzal, A. J., Ning, Y., Wang, R., Bellizzi, M., Valent, B., and Wang, G.-L. (2012) The *Magnaporthe oryzae* effector AvrPiz-t targets the RING E3 ubiquitin ligase APIP6 to suppress pathogen-associated molecular pattern–triggered immunity in rice. *Plant Cell* **24**, 4748

9. Park, C. H., Shirsekar, G., Bellizzi, M., Chen, S., Songkumarn, P., Xie, X., Shi, X., Ning, Y., Zhou, B., Suttiviriya, P., Wang, M., Umemura, K., and Wang, G.-L. (2016) The E3 ligase APIP10 connects the effector AvrPiz-t to the NLR receptor Piz-t in rice. *PLoS Pathog.* **12**, e1005529

10. Tang, M., Ning, Y., Shu, X., Dong, B., Zhang, H., Wu, D., Wang, H., Wang, G.-L., and Zhou, B. (2017) The Nup98 homolog APIP12 targeted by the effector AvrPiz-t is involved in rice basal resistance against *Magnaporthe oryzae*. *Rice (N. Y.)* **10**, 5

11. Wang, R., Ning, Y., Shi, X., He, F., Zhang, C., Fan, J., Jiang, N., Zhang, Y., Zhang, T., Hu, Y., Bellizzi, M., and Wang, G. L. (2016) Immunity to rice blast disease by suppression of effector-triggered necrosis. *Curr. Biol.* **26**, 2399–2411

12. Orbach, M. J., Farrall, L., Sweigard, J. A., Chumley, F. G., and Valent, B. (2000) A telomeric avirulence gene determines efficacy for the rice blast resistance gene Pi-ta. *Plant Cell* **12**, 2019–2032

13. Jia, Y., McAdams, S. A., Bryan, G. T., Hershey, H. P., and Valent, B. (2000) Direct interaction of resistance gene and avirulence gene products confers rice blast resistance. *EMBO J.* **19**, 4004–4014

14. Jones, J. D. G., Vance, R. E., and Dangl, J. L. (2016) Intracellular innate immune surveillance devices in plants and animals. *Science* **354**, aaf6395

15. Jones, J. D. G., and Dangl, J. L. (2006) The plant immune system. *Nature* **444**, 323–329

16. van der Hoorn, R. A. L., and Kamoun, S. (2008) From Guard to Decoy: A new model for perception of plant pathogen effectors. *Plant Cell* **20**, 2009–2017

17. Dangl, J. L., and Jones, J. D. (2001) Plant pathogens and integrated defence responses to infection. *Nature* **411**, 826–833

18. Collier, S. M., Hamel, L. P., and Moffett, P. (2011) Cell death mediated by the N-terminal domains of a unique and highly conserved class of NB-LRR protein. *Mol. Plant Microbe Interact.* **24**, 918–931

19. Pan, Q., Wendel, J., and Fluhr, R. (2000) Divergent evolution of plant NBS-LRR resistance gene homologues in dicot and cereal genomes. *J. Mol. Evol.* **50**, 203–213

20. Takken, F. L. W., Albrecht, M., and Tameling, W. I. L. (2006) Resistance proteins: Molecular switches of plant defence. *Curr. Opin. Plant Biol.* **9**, 383–390

21. Tameling, W. I. L., Elzinga, S. D. J., Darmin, P. S., Vossen, J. H., Takken, F. L. W., Haring, M. A., and Cornelissen, B. J. C. (2002) The tomato R gene products I-2 and Mi-1 are functional ATP binding proteins with ATPase activity. *Plant Cell* **14**, 2929–2939

22. Cesari, S., Thilliez, G., Ribot, C., Chalvon, V., Michel, C., Jauneau, A., Rivas, S., Alaux, L., Kanzaki, H., Okuyama, Y., Morel, J.-B., Fournier, E., Tharreau, D., Terauchi, R., and Kroj, T. (2013) The rice resistance protein pair RGA4/RGA5 recognizes the *Magnaporthe oryzae* effectors AVR-Pia and AVR1-CO39 by direct binding. *Plant Cell* **25**, 1463

23. Sarris, P. F., Cevik, V., Dagdas, G., Jones, J. D. G., and Krasileva, K. V. (2016) Comparative analysis of plant immune receptor architectures uncovers host proteins likely targeted by pathogens. *BMC Biol.* **14**, 1–19

24. Kroj, T., Chanclud, E., Michel-Romiti, C., Grand, X., and Morel, J.-B. (2016) Integration of decoy domains derived from protein targets of pathogen effectors into plant immune receptors is widespread. *New Phytol.* **210**, 618–626

25. Cesari, S., Bernoux, M., Moncuquet, P., Kroj, T., and Dodds, P. N. (2014) A novel conserved mechanism for plant NLR protein pairs: The "integrated decoy" hypothesis. *Front. Plant Sci.* **5**, 606

26. Wu, C.-H., Krasileva, K. V., Banfield, M. J., Terauchi, R., and Kamoun, S. (2015) The "sensor domains" of plant NLR proteins: More than decoys? *Front. Plant Sci.* **6**, 134

27. Ashikawa, I., Hayashi, N., Yamane, H., Kanamori, H., Wu, J., Matsumoto, T., Ono, K., and Yano, M. (2008) Two adjacent nucleotide-binding site-leucine-rich repeat class genes are required to confer Pikm-specific rice blast resistance. *Genetics* **180**, 2267–2276

28. Kanzaki, H., Yoshida, K., Saitoh, H., Fujisaki, K., Hirabuchi, A., Alaux, L., Fournier, E., Tharreau, D., and Terauchi, R. (2012) Arms race co-evolution of *Magnaporthe oryzae* AVR-Pik and rice Pik genes driven by their physical interactions. *Plant J.* **72**, 894–907

29. Maqbool, A., Saitoh, H., Franceschetti, M., Stevenson, C. E. M., Uemura, A., Kanzaki, H., Kamoun, S., Terauchi, R., and Banfield, M. J. (2015) Structural basis of pathogen recognition by an integrated HMA domain in a plant NLR immune receptor. *Elife* **4**, e08709

30. Yuan, B., Zhai, C., Wang, W., Zeng, X., Xu, X., Hu, H., Lin, F., Wang, L., and Pan, Q. (2011) The Pik-p resistance to *Magnaporthe oryzae* in rice is mediated by a pair of closely linked CC-NBS-LRR genes. *Theor. Appl. Genet.* **122**, 1017–1028

31. Zhai, C., Lin, F., Dong, Z., He, X., Yuan, B., Zeng, X., Wang, L., and Pan, Q. (2011) The isolation and characterization of Pik, a rice blast resistance gene which emerged after rice domestication. *New Phytol.* **189**, 321–334

32. Zhai, C., Zhang, Y., Yao, N., Lin, F., Liu, Z., Dong, Z., Wang, L., and Pan, Q. (2014) Function and interaction of the coupled genes responsible for Pik-h encoded rice blast resistance. *PLoS One* **9**, e98067

33. Guo, L., Cesari, S., de Guillen, K., Chalvon, V., Mammri, L., Ma, M., Meusnier, I., Bonnot, F., Padilla, A., Peng, Y.-L., Liu, J., and Kroj, T. (2018) Specific recognition of two MAX effectors by integrated HMA domains in plant immune receptors involves distinct binding surfaces. *Proc. Natl. Acad. Sci. U. S. A.* **115**, 11637

34. Oikawa, K., Fujisaki, K., Shimizu, M., Takeda, T., Saitoh, H., Hirabuchi, A., Białas, A., Langner, T., Kellner, R., Bozkurt, T. O., Cesari, S., Kroj, T., Maidment, J. H. R., Banfield, M. J., Kamoun, S., *et al.* (2020) The blast pathogen effector AVR-Pik binds and stabilizes rice heavy metal-associated (HMA) proteins to co-opt their function in immunity. *bioRxiv*. https://doi.org/10.1101/2020.12.01.406389

35. Yoshida, K., Saitoh, H., Fujisawa, S., Kanzaki, H., Matsumura, H., Yoshida, K., Tosa, Y., Chuma, I., Takano, Y., Win, J., Kamoun, S., and Terauchi, R. (2009) Association genetics reveals three novel avirulence genes from the rice blast fungal pathogen *Magnaporthe oryzae*. *Plant Cell* **21**, 1573–1591

36. Wu, W., Wang, L., Zhang, S., Li, Z., Zhang, Y., Lin, F., and Pan, Q. (2014) Stepwise arms race between AvrPik and Pik alleles in the rice blast pathosystem. *Mol. Plant Microbe Interact.* **27**, 759–769

37. Longya, A., Chaipanya, C., Franceschetti, M., Maidment, J. H. R., Banfield, M. J., and Jantasuriyarat, C. (2019) Gene duplication and mutation in the emergence of a novel aggressive allele of the AVR-Pik effector in the rice blast fungus. *Mol. Plant Microbe Interact.* **32**, 740–749

38. De la Concepcion, J. C., Maidment, J. H. R., Longya, A., Xiao, G., Franceschetti, M., and Banfield, M. J. (2020) The allelic rice immune receptor Pikh confers extended resistance to strains of the blast fungus through a single polymorphism in the effector binding interface. *bioRxiv*. https://doi.org/10.1101/2020.09.05.284240

39. de Abreu-Neto, J. B., Turchetto-Zolet, A. C., de Oliveira, L. F. V., Bodanese Zanettini, M. H., and Margis-Pinheiro, M. (2013) Heavy metal-associated isoprenylated plant protein (HIPP): Characterization of a family of proteins exclusive to plants. *FEBS J.* **280**, 1604–1616

40. Khan, I. U., Rono, J. K., Zhang, B. Q., Liu, X. S., Wang, M. Q., Wang, L. L., Wu, X. C., Chen, X., Cao, H. W., and Yang, Z. M. (2019) Identification of novel rice (*Oryza sativa*) HPP and HIPP genes tolerant to heavy metal toxicity. *Ecotoxicol. Environ. Saf.* **175**, 8–18

41. De la Concepcion, J. C., Franceschetti, M., MacLean, D., Terauchi, R., Kamoun, S., and Banfield, M. J. (2019) Protein engineering expands the effector recognition profile of a rice NLR immune receptor. *Elife* **8**, e47713

ASBMB

42. De la Concepcion, J. C., Franceschetti, M., Maqbool, A., Saitoh, H., Terauchi, R., Kamoun, S., and Banfield, M. J. (2018) Polymorphic residues in an allelic rice NLR expand binding and response to effectors of the blast pathogen. *Nat. Plants* **4**, 576–585

43. Dagdas, Y. F., Belhaj, K., Maqbool, A., Chaparro-Garcia, A., Pandey, P., Petre, B., Tabassum, N., Cruz-Mireles, N., Hughes, R. K., Sklenar, J., Win, J., Menke, F., Findlay, K., Banfield, M. J., Kamoun, S., *et al.* (2016) An effector of the Irish potato famine pathogen antagonizes a host autophagy cargo receptor. *Elife* **5**, 23

44. Maqbool, A., Hughes, R. K., Dagdas, Y. F., Tregidgo, N., Zess, E., Belhaj, K., Round, A., Bozkurt, T. O., Kamoun, S., and Banfield, M. J. (2016) Structural basis of host autophagy-related protein 8 (ATG8) binding by the Irish potato famine pathogen effector protein PexRD54. *J. Biol. Chem.* **291**, 20270–20282

45. de Guillen, K., Ortiz-Vallejo, D., Gracy, J., Fournier, E., Kroj, T., and Padilla, A. (2015) Structure analysis uncovers a highly diverse but structurally conserved effector family in phytopathogenic fungi. *PLoS Pathog.* **11**, e1005228

46. Emsley, P., Lohkamp, B., Scott, W. G., and Cowtan, K. (2010) Features and development of Coot. *Acta Crystallogr. D Biol. Crystallogr.* **66**, 486–501

47. Ortiz, D., de Guillen, K., Cesari, S., Chalvon, V., Gracy, J., Padilla, A., and Kroj, T. (2017) Recognition of the *Magnaporthe oryzae* effector AVR-Pia by the decoy domain of the rice NLR immune receptor RGA5. *Plant Cell* **29**, 156

48. Weßling, R., Epple, P., Altmann, S., He, Y., Yang, L., Henz, S. R., McDonald, N., Wiley, K., Bader, K. C., Gläßer, C., Mukhtar, M. S., Haigis, S., Ghamsari, L., Stephens, A. E., Ecker, J. R., *et al.* (2014) Convergent targeting of a common host protein-network by pathogen effectors from three kingdoms of life. *Cell Host Microbe* **16**, 364–375

49. Cowan, G. H., Roberts, A. G., Jones, S., Kumar, P., Kalyandurg, P. B., Gil, J. F., Savenkov, E. I., Hemsley, P. A., and Torrance, L. (2018) Potato mop-top virus co-opts the stress sensor HIPP26 for long-distance movement. *Plant Physiol.* **176**, 2052–2070

50. Radakovic, Z. S., Anjam, M. S., Escobar, E., Chopra, D., Cabrera, J., Silva, A. C., Escobar, C., Sobczak, M., Grundler, F. M. W., and Siddique, S. (2018) Arabidopsis HIPP27 is a host susceptibility gene for the beet cyst nematode *Heterodera schachtii*. *Mol. Plant Pathol.* **19**, 1917–1928

51. Sarris, P. F., Duxbury, Z., Huh, S. U., Ma, Y., Segonzac, C., Sklenar, J., Derbyshire, P., Cevik, V., Rallapalli, G., Saucet, S. B., Wirthmueller, L., Menke, F. L. H., Sohn, K. H., and Jones, J. D. G. (2015) A plant immune receptor detects pathogen effectors that target WRKY transcription factors. *Cell* **161**, 1089–1100

52. Saucet, S. B., Ma, Y., Sarris, P. F., Furzer, O. J., Sohn, K. H., and Jones, J. D. G. (2015) Two linked pairs of Arabidopsis TNL resistance genes independently confer recognition of bacterial effector AvrRps4. *Nat. Commun.* **6**, 6338

53. Deslandes, L., Olivier, J., Peeters, N., Feng, D. X., Khounlotham, M., Boucher, C., Somssich, I., Genin, S., and Marco, Y. (2003) Physical interaction between RRS1-R, a protein conferring resistance to bacterial wilt, and PopP2, a type III effector targeted to the plant nucleus. *Proc. Natl. Acad. Sci. U. S. A.* **100**, 8024

54. Cesari, S. (2018) Multiple strategies for pathogen perception by plant immune receptors. *New Phytol.* **219**, 17–24

55. Chaipanya, C., Telebanco-Yanoria, M. J., Quime, B., Longya, A., Korinsak, S., Korinsak, S., Toojinda, T., Vanavichit, A., Jantasuriyarat, C., and Zhou, B. (2017) Dissection of broad-spectrum resistance of the Thai rice variety Jao Hom Nin conferred by two resistance genes against rice blast. *Rice* **10**, 18

56. Wongsaprom, C., Sirithunya, P., Vanavichit, A., Pantuwan, G., Jongdee, B., Sidhiwong, N., Lanceras-Siangliw, J., and Toojinda, T. (2010) Two introgressed quantitative trait loci confer a broad-spectrum resistance to blast disease in the genetic background of the cultivar RD6 a Thai glutinous jasmine rice. *Field Crops Res.* **119**, 245–251

57. Khanthong, S., Kate-Ngam, S., Riabroy, K., Siangliw, J., and Toojinda, T. (2018) Development of aromatic glutinous rice for rainfed lowland areas by marker assisted selection. *Chiang Mai J. Sci.* **45**, 2312–2321

58. Berrow, N. S., Alderton, D., Sainsbury, S., Nettleship, J., Assenberg, R., Rahman, N., Stuart, D. I., and Owens, R. J. (2007) A versatile ligation-independent cloning method suitable for high-throughput expression screening applications. *Nucleic Acids Res.* **35**, e45

59. Lobstein, J., Emrich, C. A., Jeans, C., Faulkner, M., Riggs, P., and Berkmen, M. (2012) SHuffle, a novel *Escherichia coli* protein expression strain capable of correctly folding disulfide bonded proteins in its cytoplasm. *Microb. Cell Fact.* **11**, 56

60. Studier, F. W. (2005) Protein production by auto-induction in high density shaking cultures. *Protein Expr. Purif.* **41**, 207–234

61. Vonrhein, C., Flensburg, C., Keller, P., Sharff, A., Smart, O., Paciorek, W., Womack, T., and Bricogne, G. (2011) Data processing and analysis with the autoPROC toolbox. *Acta Crystallogr. D Biol. Crystallogr.* **67**, 293–302

62. Evans, P. R., and Murshudov, G. N. (2013) How good are my data and what is the resolution? *Acta Crystallogr. D Biol. Crystallogr.* **69**, 1204–1214

63. McCoy, A. J., Grosse-Kunstleve, R. W., Adams, P. D., Winn, M. D., Storoni, L. C., and Read, R. J. (2007) Phaser crystallographic software. *J. Appl. Crystallogr.* **40**, 658–674

64. Cowtan, K. (2006) The Buccaneer software for automated model building. 1. Tracing protein chains. *Acta Crystallogr. D Biol. Crystallogr.* **62**, 1002–1011

65. Murshudov, G. N., Skubák, P., Lebedev, A. A., Pannu, N. S., Steiner, R. A., Nicholls, R. A., Winn, M. D., Long, F., and Vagin, A. A. (2011) REFMAC5 for the refinement of macromolecular crystal structures. *Acta Crystallogr. D Biol. Crystallogr.* **67**, 355–367

66. Winn, M. D., Ballard, C. C., Cowtan, K. D., Dodson, E. J., Emsley, P., Evans, P. R., Keegan, R. M., Krissinel, E. B., Leslie, A. G. W., McCoy, A., McNicholas, S. J., Murshudov, G. N., Pannu, N. S., Potterton, E. A., Powell, H. R., *et al.* (2011) Overview of the CCP4 suite and current developments. *Acta Crystallogr. D Biol. Crystallogr.* **67**, 235–242

67. Chen, V. B., Arendall, W. B., III, Headd, J. J., Keedy, D. A., Immormino, R. M., Kapral, G. J., Murray, L. W., Richardson, J. S., and Richardson, D. C. (2010) MolProbity: All-atom structure validation for macromolecular crystallography. *Acta Crystallogr. D Biol. Crystallogr.* **66**, 12–21

68. Krissinel, E., and Henrick, K. (2007) Inference of macromolecular assemblies from crystalline state. *J. Mol. Biol.* **372**, 774–797

69. McNicholas, S., Potterton, E., Wilson, K. S., and Noble, M. E. (2011) Presenting your structures: The CCP4mg molecular-graphics software. *Acta Crystallogr. D Biol. Crystallogr.* **67**, 386–394

70. Krissinel, E. (2015) Stock-based detection of protein oligomeric states in jsPISA. *Nucleic Acids Res.* **43**, W314–W319

71. Wickham, H. (2016) *ggplot2: Elegant Graphics for Data Analysis.* Springer-Verlag, New York

72. R Core Development Team (2018) *R: A Language and Environment for Statistical Computing.* R Foundation for Statistical Computing, Vienna, Austria